



CHORUS

This is the accepted manuscript made available via CHORUS. The article has been published as:

Microelectrokinetic turbulence in microfluidics at low Reynolds number

Guiren Wang, Fang Yang, and Wei Zhao

Phys. Rev. E **93**, 013106 — Published 6 January 2016

DOI: [10.1103/PhysRevE.93.013106](https://doi.org/10.1103/PhysRevE.93.013106)

Micro-electrokinetic turbulence in microfluidics at low Reynolds number

Guiren Wang,^{*,1,2} Fang Yang,^{#,1} Wei Zhao^{#,1,3}

[#]These authors have equal contribution to this work; ¹Department of Mechanical Engineering,

²Biomedical Engineering Program, University of South Carolina, Columbia, SC 29208, USA.³

Institute of Photonics and Photo-technology, International Scientific and Technological Cooperation Base of Photoelectric Technology and Functional Materials and Application, Northwest University, 229 North Taibai Rd, Xi'an 710069, People's Republic of China. * guirenwang@sc.edu

There is commonly no turbulence in microfluidics, and the flows are believed to be either laminar or chaotic, since Reynolds number (Re) in microflows is usually on the order of unity or lower. However, we recently demonstrated that, it is possible to achieve turbulence with low Re (based on the measured flow velocity and the width of the channel entrance) when a pressure driven flow is electrokinetically forced in a quasi T-microchannel. To be able to measure high frequency velocity fluctuations in microchannels, a novel velocimeter with submicrometer spatial resolution and microsecond temporal resolution, called Laser Induced Fluorescence Photobleaching Anemometer (LIFPA), is developed. Here we characterize the micro electrokinetic turbulence (μ EKT) and observe some typical and important features of high Re flows, such as Kolmogorov $-5/3$ spectrum of velocity fluctuation, which usually can be realized only at very high Re in macro turbulent flows.

I. Introduction

Turbulence is commonly viewed as a type of macroflow phenomenon under sufficiently high Reynolds number (Re). One of the most successful progresses in turbulence research is Kolmogorov's prediction of the existence of universal statistical features of small-scale structures in fully developed turbulent flows, e.g. $-5/3$ slope in power spectrum of velocity (PSV). To achieve these universal behaviors, Re has to be very high [1]. On the other hand, it has been widely perceived in science, engineering and medicine that there is never any turbulence in low Re flow for Newtonian fluids [2]. Consequently, it is commonly believed that in microfluidics flows can only be laminar or chaotic under forcing either passively or actively [3], as the Re in micro-devices is normally below or on the order of unity, even if electrokinetic (EK) forcing has been applied to increase flow instability [4-6].

Interesting is that, recently, we have demonstrated there can be turbulence in microfluidics where the bulk flow Re is and when a pressure driven flow is electrokinetically forced by increasing nominal electric Grashof number (Gr_e) [7]. The further questions are how to characterize the micro electrokinetic turbulence (μ EKT) and what are the features of the μ EKT. To understand statistical features and multiscale spatial structures, especially the small-scale structures of turbulent flows in microchannels, it is necessary to

measure the statistical features of flow velocity fluctuations with sufficiently high spatial and temporal resolution simultaneously.

Ideally, Micro Particle Imaging Velocimetry (μ PIV) should be used to measure the spatial spectrum of velocity. Unfortunately it is impossible to measure the spatial spectrum with reasonable resolution and bandwidth for current μ PIV as explained before for the μ EKT [8]. Standard μ PIV has difficulty in measuring velocity in highly fluctuated microflows with high frequency, since the velocity measurement in these flows requires simultaneously high spatial and temporal resolution. Furthermore, in electrokinetic flows, particles' velocities are essentially different from that of the local flow and μ PIV is not be able to measure flow velocity reliably. Some other flow diagnostic methods are also developed in microfluidics, such as Molecular Tagging Velocimetry (MTV)[9,10], Hot-Wire Anemometer (HWA) and its derivatives [11], Laser Doppler Velocimetry (LDV) [12] etc. However, to our knowledge, they all have intrinsic disadvantages on measuring velocity fluctuations with high frequency in the μ EKT. For example, MTV is slow and can only measure slowly varying flow. Although HWA and its derivatives can measure high frequency signal, they cannot measure flow velocities at the positions away from walls, as they are fabricated on the microchannel's wall. Moreover, HWA are inaccurate, since to heat the wire they requires an extra electric current, which can interfere the electrokinetic flows.

LDV can have high temporal resolution, but its measuring volume is, to the best of authors' knowledge, larger than 4 μm by 16 μm [13]. The corresponding spatial resolution is also too low to measure the μEKT that we plan to show in the present work.

Due to these reasons, we have developed a new confocal submicroscopic velocimeter, called Laser Induced Fluorescence Photobleaching Anemometer (LIFPA) to measure velocity fluctuation. The technique is based on the relation between fluorescence intensity and flow velocity because of the photobleaching mechanism of fluorescent dyes [14]. LIFPA is a non-invasive method and has a high spatiotemporal resolution. When neutral and small molecular dyes are used as tracer, the aforementioned problems resulted from particle tracers can be avoided.

Here, we report our experimental characterization of some statistical features of the aforementioned μEKT observed recently at low Re in a microchannel. It is astonishingly found that the μEKT also exhibits some statistical features of the small-scale structures in high Re macro turbulent flows. The confocal LIFPA is used to measure the velocity fluctuations.

II. Principle of generating μEKT

The principle of generating and measuring the μEKT is given below to illustrate qualitatively how the μEKT can be generated. For incompressible fluids, the Navier-Stokes equation with electrokinetics can be described as

$$\rho(\partial\mathbf{u}/\partial t + \mathbf{u} \cdot \nabla\mathbf{u}) = \nabla p + \mu\nabla^2\mathbf{u} + \mathbf{F}_e \quad (1)$$

$$\mathbf{F}_e = \rho_f\mathbf{E} - \frac{1}{2}(\mathbf{E} \cdot \mathbf{E})\nabla\epsilon \quad (2)$$

$$\rho_f = \nabla \cdot (\epsilon\mathbf{E}) = \nabla\epsilon \cdot \mathbf{E} + \epsilon\nabla \cdot \mathbf{E} \quad (3)$$

where ρ , \mathbf{u} , p , μ are the fluid density, flow velocity, pressure and dynamic viscosity respectively; \mathbf{F}_e is electrical body force, which consists of the Coulomb force and dielectric force respectively in incompressible fluids; \mathbf{E} is electric field, ρ_f is the free charge density in solution, where ϵ and σ are the electric permittivity and conductivity of the electrolyte respectively [5].

Let us consider a flow where the convection \mathbf{u} is small and the transport of free charge is primarily dominated by \mathbf{E} . The transport equation of free charges, i.e. $\partial\rho_f/\partial t + \nabla \cdot (\sigma\mathbf{E}) + \nabla \cdot (\rho_f\mathbf{u}) = 0$ [15], can be simplified as:

$$\partial\rho_f/\partial t + \nabla \cdot (\sigma\mathbf{E}) = 0 \quad (4)$$

Substitution of Eq. (3) into (4), combined with the fact that $\partial\epsilon/\partial t \sim 0$ (ϵ is a function of fluid temperature which is almost constant adjacent to the entrance of the channel), yields:

$$\nabla \cdot \mathbf{E} \approx - \left(\nabla\sigma \cdot \mathbf{E} + \nabla\epsilon \cdot \frac{\partial\mathbf{E}}{\partial t} + \epsilon\nabla \cdot \frac{\partial\mathbf{E}}{\partial t} \right) / \sigma \quad (5)$$

Substituted back into Eq. (2) and (3), we find:

$$\mathbf{F}_e = (\nabla\epsilon \cdot \mathbf{E})\mathbf{E} - \epsilon \frac{\nabla\sigma \cdot \mathbf{E}}{\sigma} \mathbf{E} - \epsilon \frac{\nabla\epsilon \cdot \frac{\partial\mathbf{E}}{\partial t}}{\sigma} \mathbf{E} - \frac{\epsilon^2 \nabla \cdot \frac{\partial\mathbf{E}}{\partial t}}{\sigma} \mathbf{E} - \frac{1}{2}(\mathbf{E} \cdot \mathbf{E})\nabla\epsilon \quad (6)$$

As two streams with different σ meet together, the interface between the two streams can be assumed to be frozen within a short distance before the flow starts to develop. Thus, the temperature variation due to electrothermal effects is insignificant and $\nabla\epsilon$ has negligible influence. Therefore, the first, third and fifth terms can be ignored. The initial \mathbf{F}_e can be approximately determined by:

$$\mathbf{F}_e = -\epsilon \frac{\nabla\sigma \cdot \mathbf{E}}{\sigma} \mathbf{E} - \frac{\epsilon^2}{\sigma} \left(\nabla \cdot \frac{\partial\mathbf{E}}{\partial t} \right) \mathbf{E} \quad (7)$$

Let $\mathbf{u} = U_c\hat{\mathbf{u}}$, $t = \tau\hat{t}$, $\mathbf{x} = U_c\tau\hat{\mathbf{x}}$, $\nabla = \hat{\nabla}/U_c\tau$, $\sigma = \sigma_0\hat{\sigma}$, $\mathbf{E} = E_0\hat{\mathbf{E}}$, $p = \rho U_c^2$, $\epsilon = \epsilon_{ref}\hat{\epsilon}$, where $\hat{\mathbf{u}}$, $\hat{\mathbf{x}}$, $\hat{\nabla}$ and $\hat{\mathbf{E}}$ are dimensionless functions of \mathbf{u} , \mathbf{x} , ∇ and \mathbf{E} , respectively. U_c is a characteristic velocity, τ denotes the time scale of flow, σ_0 is the initial characteristic σ of the flow, $E_0 = V_f/\sqrt{2}w$ represents the nominal \mathbf{E} across the channel width (where V_f is the applied peak-to-peak voltage between two electrodes), ϵ_{ref} is the ϵ of water at a reference temperature and w is the width of the channel at the entrance, respectively. When the angular frequency of forcing $\omega = 2\pi f_f$ (f_f is forcing frequency) is much higher than the velocity response frequency, the characteristic time scale of \mathbf{E} is $1/\omega$, not τ . Then $\partial\mathbf{E}/\partial t \sim \omega E_0 \partial\hat{\mathbf{E}}/\partial\hat{t}$. Furthermore, at the entrance, we can use $\sigma_2 - \sigma_1$ ($\sigma_2 > \sigma_1$) and σ_1 to qualitatively replace $\Delta\sigma_0$ and σ_0 without losing physical meaning. Here σ_1 and σ_2 are σ of the stream 1 and 2 respectively. Then, we have:

$$\mathbf{F}_e \sim - \frac{\epsilon_{ref}(\sigma_2 - \sigma_1)E_0^2}{\sigma_1 U_c \tau} \hat{\epsilon} \frac{\hat{\nabla} \cdot \hat{\mathbf{E}}}{\hat{\sigma}} \hat{\mathbf{E}} - \frac{\epsilon_{ref}^2 \omega E_0^2}{\sigma_1 U_c \tau} \hat{\epsilon}^2 \frac{\hat{\nabla} \cdot \frac{\partial\hat{\mathbf{E}}}{\partial\hat{t}}}{\hat{\sigma}} \hat{\mathbf{E}} \quad (8)$$

while the first term of Eq. (8) is consistent with the result in DC case [4], the second term is related to the initial \mathbf{F}_e due to AC \mathbf{E} . However, in practice, to satisfy quasi-electrostatic condition, normally $\varepsilon_{ref}\omega < \sigma_1 < \sigma_2 - \sigma_1$. The 2nd term of Eq. (8) should be much smaller than the 1st term, and can be neglected. This may also indicate the μ EKT under DC forcing is more violent than that under AC forcing at the same voltage. Therefore,

$$\mathbf{F}_e \sim -\frac{\varepsilon_{ref}(\sigma_2 - \sigma_1)E_0^2}{\sigma_1 U_c \tau} \hat{\varepsilon} \frac{\widehat{\nabla \sigma} \cdot \widehat{\mathbf{E}}}{\widehat{\sigma}} \widehat{\mathbf{E}} \quad (9)$$

Substitute Eq. (9) in Eq. (1) with dimensionless format, we have:

$$\begin{aligned} & \rho \frac{U_c}{\tau} \left(\frac{\partial \widehat{\mathbf{u}}}{\partial \widehat{t}} + \widehat{\mathbf{u}} \cdot \widehat{\nabla} \widehat{\mathbf{u}} \right) = \\ & -\rho \frac{U_c}{\tau} \widehat{\nabla} \widehat{\mathbf{p}} - \frac{\varepsilon_{ref}(\sigma_2 - \sigma_1)E_0^2}{\sigma_1 U_c \tau} \hat{\varepsilon} \frac{\widehat{\nabla \sigma} \cdot \widehat{\mathbf{E}}}{\widehat{\sigma}} \widehat{\mathbf{E}} + \frac{\mu}{U_c \tau^2} \widehat{\nabla}^2 \widehat{\mathbf{u}} \end{aligned} \quad (10)$$

Initially, at a large scale where the influence of fluid viscosity is small, \mathbf{F}_e directly drives and causes the strong electrokinetic (EK) flow. The order of the corresponding velocity can be reached by balancing the inertial term and \mathbf{F}_e in Eq. (10) as $U_e = \sqrt{\varepsilon_{ref}(\sigma_2 - \sigma_1)E_0^2 / \rho \sigma_1}$. Using U_e as the characteristic velocity scale and substituting it in Eq. (10), we have:

$$\left(\frac{\partial \widehat{\mathbf{u}}}{\partial \widehat{t}} + \widehat{\mathbf{u}} \cdot \widehat{\nabla} \widehat{\mathbf{u}} \right) = -\widehat{\nabla} \widehat{\mathbf{p}} - \frac{(\widehat{\nabla \sigma} \cdot \widehat{\mathbf{E}})}{\widehat{\sigma}} \widehat{\mathbf{E}} + \frac{1}{\sqrt{Gr_e}} \widehat{\nabla}^2 \widehat{\mathbf{u}} \quad (11)$$

where $Gr_e = \rho \varepsilon_{ref} d^2 E_0^2 (\sigma_2 - \sigma_1) / \sigma_1 \mu^2$ is the nominal electric Grashof number. Here, $d = w$. It can be seen that, by increasing the initial σ_2 / σ_1 , E_0 and parallelizing $\nabla \sigma$ and \mathbf{E} , Gr_e can be enhanced while keeping the influence of viscous force relatively inhibited, thus making the μ EKT possible. For instance, when the bulk flow velocity $U_b = 3$ mm/s, $\rho = 10^3$ kg/m³, $\mu = 10^{-3}$ kg/m·s, $\varepsilon_{ref} = 80.2 \times 8.854 \times 10^{-12}$ F/m, $\sigma_1 = 1$ μ S/cm, $\sigma_2 / \sigma_1 = 5000$, $E_0 = 1 \times 10^5$ V/m, the corresponding viscous force without forcing is estimated to be on the order of 7×10^2 N/m³, and Gr_e is 7.1×10^5 . If we use $\sigma = (\sigma_1 + \sigma_2) / 2$ as the reference value, the initial interfacial distance Δy between the two streams is 1 μ m, and the first term on the right side of Eq. (7) can approximate \mathbf{F}_e in Eq. (1), i.e. $\mathbf{F}_e \sim 2\varepsilon_{ref}(\sigma_2 - \sigma_1)E_0^2 / ((\sigma_1 + \sigma_2)\Delta y)$, then \mathbf{F}_e in Eq. (1) is estimated to be on the order of 1×10^7 N/m³. Thus, \mathbf{F}_e can overcome viscous force to generate the μ EKT.

Since in liquids, Schmidt number ($Sc = \mu / \rho D_e$, where D_e is the effective diffusivity of ions) is large, σ diffusion will be much slower than the momentum diffusion. σ structures can be sustained to Batchelor scale by the interaction between inertial and viscous forces, with approximately a constant flux of scalar variance. Therefore, σ ratio on each local interface of σ structure will be nearly constant in the range from large scale to Batchelor scale. This implies \mathbf{F}_e can be approximately sustained to very small scales. In other words, the energy could be injected through a wide scale range. Hence, at a specific length scale l , where the time scale of convection under forcing ($\tau_e = l / U_e$) is equal to the corresponding viscous diffusion time scale ($\tau_d = \rho l^2 / \mu$), a nominal electric Kolmogorov scale in the μ EKT can be qualitatively concluded:

$$\begin{aligned} l_{ed} &= \sqrt{\mu^2 \sigma_1 / \rho \varepsilon_{ref} E_0^2 (\sigma_2 - \sigma_1)} = \sqrt{d^2 / Gr_e} \\ &= \sqrt{d^2 Sc / Ra_e} \end{aligned} \quad (12)$$

Here, $Ra_e = Sc Gr_e$ is the electric Rayleigh number. The larger the Gr_e (or Ra_e), the smaller l_{ed} . Therefore, one can increase Gr_e to make EK flows more unstable to generate μ EKT.

Unsteady and chaotic EK flows have been studied extensively in the past decade. In the previously published chaotic electrokinetic flows, for instance, from Santiago's group [5,6], the electrodes are mostly located at the inlet and outlet wells and there is not a splitter plate with a sharp trailing edge at the entrance of the microchannels. In this configuration, the corresponding electric field is relatively low and not parallel with the applied conductivity gradient. Furthermore, without a splitter plate and trailing edge, due to initial molecular diffusion between the two streams before they enter the electric field within the microchannels, the conductivity gradient is not high within the EK flows. Thus the resulting in electric force is also small.

Compared with previous studies, the present μ EKT is generated by enhancing \mathbf{F}_e or Gr_e through four methods: (1) paralleling the electric field to the conductivity gradient to increase $\widehat{\nabla \sigma} \cdot \widehat{\mathbf{E}}$; (2) diverging the conductive sidewalls to increase the x -component of \mathbf{E} [7] as well; (3) using a sharp trailing edge to ensure a high conductivity gradient at the entrance of the microchannel; (4) increasing the initial electric conductivity ratio and \mathbf{E} simultaneously. Large conductivity ratio not only generates large

electrokinetic force, but also causes the scalar structures more sustainable at downstream. It makes the EK force have a long-term effect on forcing the flow and enhancing the flow disturbance.

If Gr_e is sufficiently high, a nonlinear energy cascade process could be resulted in and a continuous power spectrum of turbulence could be generated, even though Re is still very low. Along with the aforementioned F_e , there can also be AC electroosmotic flow (EOF) in the transverse direction. Since σ of the two streams is different initially, the velocity of the AC EOF is different between the two streams, resulting more shear stress and secondary flow in the transverse direction in the presence of the sidewalls. In addition, electrothermal flow may also produce extra stirring in small scales downstream.

III. Experimental setup and materials

A. Microchip for EK flow

A micro diffuser with a small divergence angle of 5° is fabricated for this research. The channel was made of two transparent acrylic plastic substrates (1.25 mm thick for top and 100 μm for bottom). Different from

the top acrylic cover, the bottom one has very good UV transparency. The sidewalls of the channel were consist of two gold sheets between the substrates as electrodes. Compared with a parallel channel, this diverging channel can cause the basic flow to be more unstable and thus enhance turbulence [7]. The channel is 130 μm in width and 240 μm in height at the entrance, with a total length of 5 mm as shown in Fig. 1a. Two streams separated initially by a splitter plate with a sharp trailing edge are driven by a syringe pump and injected into the microchannel. The two pressure driven streams have identical average flow velocity. One stream is DI water which has σ_1 of 1 $\mu\text{S}/\text{cm}$. The other is buffer solution with σ_2 of 5000 $\mu\text{S}/\text{cm}$. The two streams have same flow rate of 2.0 $\mu\text{L}/\text{min}$. Without EK forcing, the corresponding Re based on the bulk flow velocity U_b and hydraulic diameter at the channel's entrance was about 0.4. 100 kHz AC voltage was applied to the two electrodes at the sidewalls to force the flows electrokinetically for all flows in this study. Although much lower ω can create more unstable flow, this high frequency signal was selected to avoid electrolysis for lab-on-a-chip application [16].

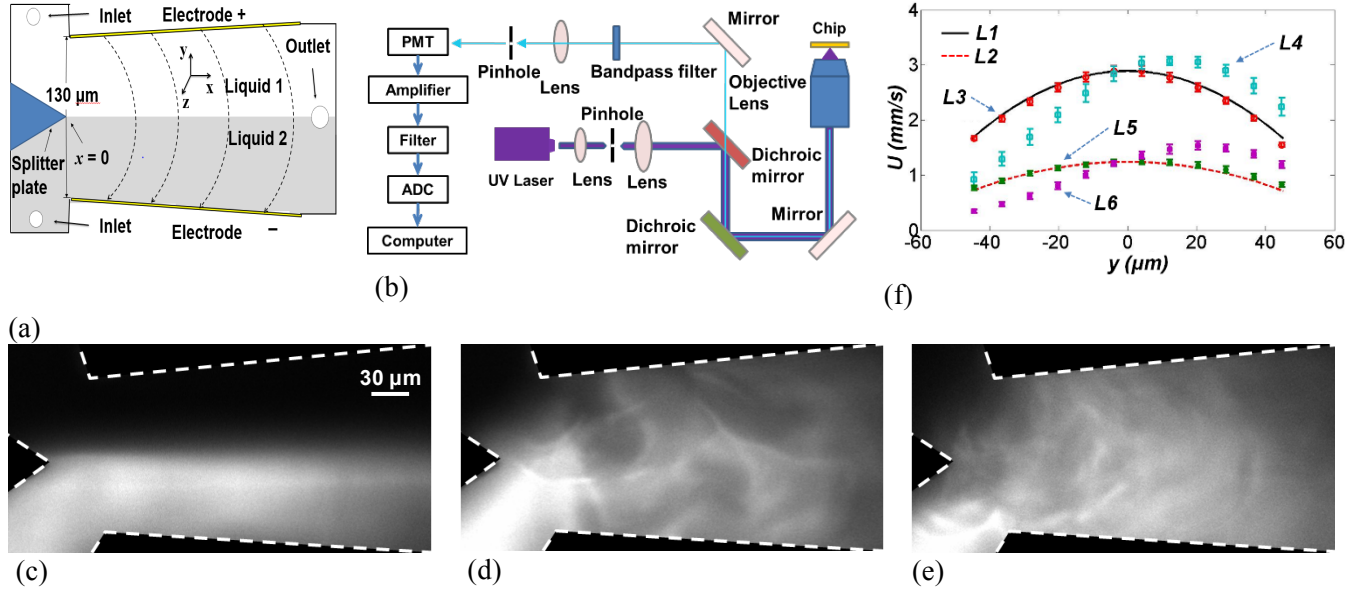


Fig. 1 (Color online) Schematic of the setup, visualization and U profile measured by μ PIV. (a) Diagram of the microchannel. $x = 0$ at the trailing edge, $y=z=0$ along the center line. (b) LIFPA setup. (c) Laminar flow without forcing. (d) $V_f = 8 V_{p-p}$. (e) $V_f = 20 V_{p-p}$. (See also supplemental material for videos of visualizations without and with forcing [17]) (f) U profile along y -direction at $x_4 = 100 \mu\text{m}$ and compared with J-H profile. Since near the side walls the optical quality is poor and SNR is low, the velocity data there are arbitrarily removed. L1 (black solid line): $z = 0$, J-H profile; L2 (red dashed line): $z = -90 \mu\text{m}$, J-H profile; L3-L6: measured by μ PIV. L3 (red circle): $z = 0 \mu\text{m}$, unforced; L4 (blue square): $z = 0 \mu\text{m}$, $20 V_{p-p}$; L5 (green dot): $z = -90 \mu\text{m}$, unforced; L6 (purple square): $z = -90 \mu\text{m}$, $20 V_{p-p}$.

B. LIFPA system for velocity measurement

Since there is no available velocimeter that can measure turbulence signals with sufficient spatiotemporal resolution required for this study, a confocal submicroscopic LIFPA with a neutral molecular dye as the tracer was developed to measure velocity [8,18,19]. The principle of this work can be illustrated with a simplified relationship between fluorescence intensity I_f and flow velocity magnitude, $u_s = \sqrt{u^2 + v^2}$ where u and v are the instantaneous velocity components in the x and y -direction, respectively. For a given dye concentration, detection volume (laser focus point) and laser intensity, due to laser induced fluorescence photobleaching, I_f depends on the fluid velocity u_s . Without flow, I_f will decay exponentially with time, i.e. $I_f \sim e^{-t/\tau}$, where t is the decay time and τ is the half decay time constant. However, with flow the decay time becomes the residence time of dye molecules within the detection volume, i.e. $t = d_f/u_s$, where d_f is the diameter of the focused laser beam at the detection volume. Thus, we

have $I_f \sim e^{d_f/u_s\tau}$. Based on this simple model, I_f increases only with the increase of u_s in LIFPA, when a fluid has a uniform concentration of a fluorescence dye.

In reality, as a system parameter τ depends on laser intensity within the detection volume, beam width, specific dye and buffer, and also buffer concentration. The parameter τ can be experimentally determined. Similar to Hot-Wire Anemometers, LIFPA can also establish a pre-calibrated polynomial relation between I_f and u_s . Then using the time series of I_f , we can calculate the statistical features of u_s . Since laser beam diameter is limited by optical diffraction, using scanning confocal microscopic principle, we can have submicrometer spatial resolution. With a fast bleaching dye, τ can be on the order of microsecond. Hence, measurements of velocity fluctuation with simultaneously ultrahigh spatial and temporal resolution can be achieved with LIFPA for the μ EKT in microchannels. After the instant velocity is measured and recorded, velocity fluctuation $u'_s = u_s - \langle u_s \rangle$ can be simply calculated, where $\langle \rangle$ denotes ensemble average.

A schematic of the LIFPA system is shown in Fig. 1b. A 50 mW cw laser of 405 nm wavelength was used for LIFPA. The beam was expanded and then focused to the detection point by a 100X objective (PlanApo, NA 1.4 oil immersion, Olympus, NY). A photomultiplier (R928, Hamamatsu, Japan) was used to capture the fluorescence signal. For all velocity measurement, the initial two streams of water solutions had the same neutral dye (Coumarin 102) concentration of 20 μM , but different σ . A photomultiplier tube was used as the detector to measure the fluorescence signal. The spatial resolution of the LIFPA is approximately determined by the focused laser beam volume (whose diameter and length are determinate by optical diffraction limit), which is estimated to be $(203 \text{ nm})^2 \times 1000 \text{ nm}$. The temporal resolution of the LIFPA is better than 10 μs . The dynamic range of the LIFPA is from 0.1 mm/s to larger than 55 mm/s.

C. Micro Particle Imaging Velocimetry (μPIV)

Since the LIFPA cannot measure direction of \mathbf{u} , we used our μPIV (LaVision Inc.) only to measure the distribution of streamwise mean velocity U to investigate the basic flow in the μEKT . The μPIV system is consisted of a PCO Sensicam high sensitivity camera, NewWave SOLO III pulse laser, 60x plan objective of numerical aperture $\text{NA} = 0.85$ and Newport 3D precision translation stage. 1 μm polystyrene fluorescent particle (Thermo Scientific Fluoro-Max Red) is used as tracers. The velocity field is calculated by Davis 7 software (LaVision Inc. Germany). The interrogation window size is 64 x 64 pixels ($8.1 \times 8.1 \mu\text{m}^2$) with 50% overlap.

D. Flow visualization

To reveal spatially multiple structures of various eddies in this continuous open flow, visualization is conducted with Laser-Induced Fluorescence (LIF). In this experiment, the images are captured by a high sensitivity camera (SensiCam-QE, Cooke Corp). The stream of DI water has no dye and the other stream, which has higher σ , is filled with fluorescein solution. The concentration of the fluorescein solution is 1 μM . Since fluorescein is negatively charged and has a valance of -2, adding it into the solution can change conductivity of the solution. Therefore, for the flow visualization, solution's conductivity was measured after the fluorescein dye was added into the solution to make sure the conductivities in both streams are the

same as that used in the velocity measurement where the neutral dye Coumarin 102 is the tracer.

IV. Experimental results

A. Flow visualization

Without forcing, the flow is laminar and no vortex can be observed as shown in Fig. 1c. As forcing voltage V_f is increased to 8 V_{p-p} , the flow exhibits commonly observed chaotic behavior in Fig. 1d. However, with $V_f = 20 V_{p-p}$ (corresponding Gr_e is 7.1×10^5), multiple “violent” and random eddies with different sizes (both “large” and “small”) can be distinguished in Fig. 1e. The largest one spans almost to the entire transverse length of the channel and the smallest one is around 10 μm . The flow becomes turbulent, and the eddy motion is dramatically enhanced. Since this is an open flow and the small scalar structures are developed in a very short convection time ($\sim 3 \text{ ms}$), i.e. shorter than the turn-over time of the eddy (whose size is on the order of the channel width), which is roughly equivalent to $w/u_{rms} \sim 100 \text{ ms}$ (where rms means “root mean square”, $u_{rms} = \sqrt{u'_s{}^2}$), we can assume the velocity structures are the premise of the dye structures. In addition, due to high conductivity gradient and the high electric field generated by the sharp edge of the electrodes at the entrance, the flow disturbance is so strong that some flow structures can even rollback slightly upstream of the entrance of the channel as shown in Fig 1e.

Clearly the scalar structures in Fig. 1e are essentially different from that in Fig. 1d. The latter has mostly only stretched large scale structures. Previous work indicates that the flow in Fig. 1d is in the transitional range [7]. Therefore, the flow in Fig. 1d seems to be spatially smooth, but temporally chaotic. The flow in Fig. 1e, however, is both spatially and temporally chaotic. Note the image is not as sharp as those often seen in macroflows, since the channel itself is just on the order of 100 μm , below which molecular diffusion will smear the sharp structures rapidly. To avoid the smearing effect, the exposure time of the camera is reduced to only 100 μs .

B. Mean velocity profile

To understand the basic flow, we measured profile of streamwise average velocity U along the y direction at x_4 , as shown in Fig. 1f. Without forcing, U matches very well with the numerically calculated Jeffery-

Hamel (J-H) flow [20]. However, under forcing, for a given z -position, U is no more symmetric along y -direction, but higher on the side of the stream with lower σ , as shown by in profile L4 and L6, since E and F_e decrease with the increase of σ . In addition, compared to the unforced one, on the high σ side, U increases near the center region along y -direction, but decreases near the wall, resulting in a steeper U distribution for the forced flow. Nevertheless, on the low σ side, U distribution becomes gentler along y -direction. U near the center of the channel is about 2.9 mm/s.

C. Power spectrum density of velocity fluctuations

(1) PSD at different forcing voltages

Fig. 2a shows the PSV of u'_s , i.e. $E(f)$, where f is the frequency, for various V_f at x_4 . Without forcing, $E(f)$ is flat, resulting from background noise since there is no fluctuation of velocity. With $V_f = 10 \text{ V}_{p-p}$, $E(f)$ is increased, but not significantly. The slope of $E(f)$ in the frequency of 20 - 100 Hz is approximately -3. This is similar to the well-known temporally random but

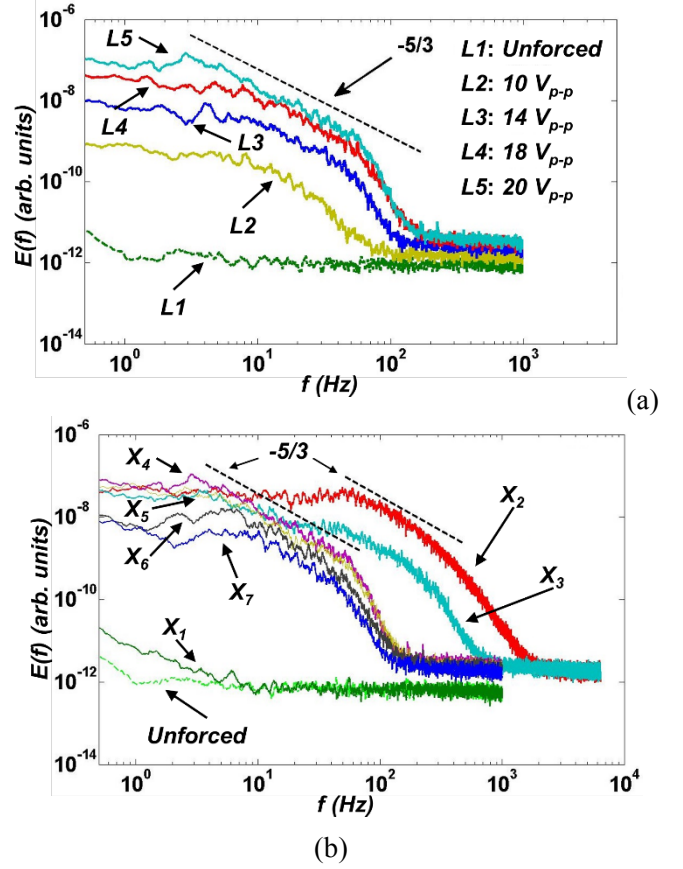


Fig. 2 (Color online) $E(f)$ under various conditions along $y = z = 0$. (a) $E(f)$ under various V at x_4 . (b) $E(f)$ development along x -direction under $V_f = 20 \text{ V}_{p-p}$. $x_1 = -10 \mu\text{m}$, $x_2 = 5 \mu\text{m}$, $x_3 = 40 \mu\text{m}$, $x_4 = 100 \mu\text{m}$, $x_5 = 200 \mu\text{m}$, $x_6 = 300 \mu\text{m}$, and $x_7 = 500 \mu\text{m}$, respectively.

spatially smooth chaotic flows, which also have a -3 slope [21,22]. When V_f is increased from 10 up to 20 V_{p-p} , $E(f)$, its bandwidth and cut-off frequency f_c where noise starts to dominate, also increase. $E(f)$ gradually develops a similar slope with the increase of V_f . Of particular interest is, at 20 V_{p-p} , the PSV is not only continuously spanned in f , but also exhibits a -5/3 slope roughly from 3 to 60 Hz in a span of more than one decade! In fact, there is already the -5/3 slope at 14 V_{p-p} , and reaches the longest bandwidth at 20 V_{p-p} (the highest V_f we can provide). This is surprising because normally the -5/3 slope corresponds to the Kolmogorov spectrum, whose existence requires Taylor Re ($Re_\lambda = u_{rms}\lambda/\nu$, where $\lambda = \sqrt{u_s'^2/(du'_s/dx)^2}$, $dx = U_b * dt$, dt is the time interval of LIFPA sampling) to be on the order of 1000 or more [23] in

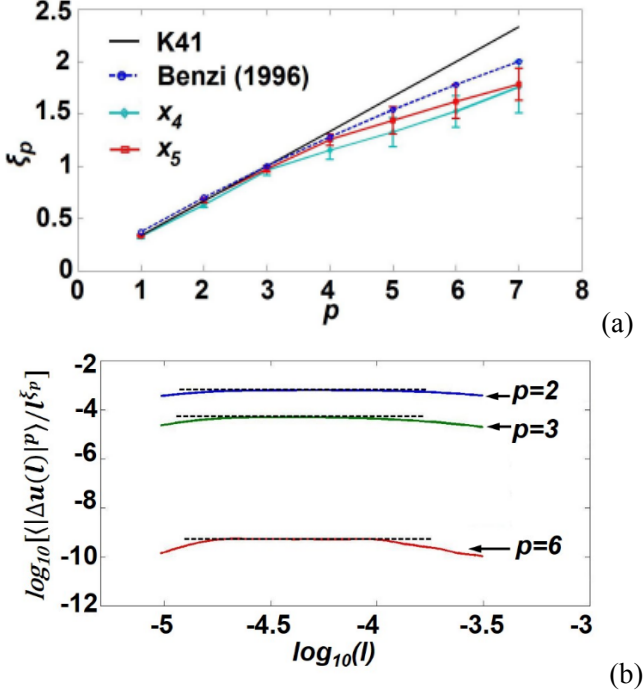


Fig. 3 (Color online) Scaling exponents of $\Delta u_s(l)$ of the flow in Fig. 1e at different positions along $y = z = 0$ and the corresponding scaling behavior at x_4 . (a) ξ_p at x_4 and x_5 . The solid line is from K41 law. The amount of data for calculating is about 10^6 , which is enough to estimate approximately up to the 7th order. (b) The scaling behaviors under three different p at x_4 .

macroflows. However, Re_λ for $20 V_{p-p}$ at x_4 is estimated to be only on the order of 0.03.

(2) PSD along different streamwise positions

Evolution of $E(f)$ along x -direction is shown in Fig. 2b. At $x_1 = -10 \mu\text{m}$, i.e. upstream of the trailing edge, $E(f)$ is almost flat and the flow remains laminar. However, at $x_2 = 5 \mu\text{m}$, the PSD changes dramatically and f_c rapidly increases to about 2 kHz. The corresponding wave number is estimated to be about $1 \times 10^6/\text{m}$. There is an energy accumulation to eddy scale up to about 50 Hz, indicating a non-equilibrium process at the entrance region. At x_2 , based on the local bulk velocity, the passage frequency of the local large scale vortex corresponding to the local channel dimensions is estimated to be around 10 Hz. Therefore, the frequencies, which are higher than the passage frequency and have $E(f)$ larger than the noise, correspond to eddies that are smaller than the transverse dimension of the channel. The higher the frequencies, the smaller the eddies. At x_3 , a narrow subrange with $-5/3$ slope from 40 to 200 Hz

appears. The $-5/3$ spectrum continues developing to x_4 with a span of more than one decade. However, f_c and $E(f)$ are lower than that upstream. At this position f_c is about 200 Hz. The reason for this could be either (1) the fast diffusion would decrease σ gradient at the interface of the two fluids, which then reduces F_e that causes the μEKT ; or (2) At x_2 , the flow has already generated smaller eddies and the corresponding σ structures, which in turn decay rapidly by the high viscous dissipation and molecular diffusion to smear the fine structures in this low Re flow. Nevertheless, it seems the energy transfer from large to small scales reaches an equilibrium, and hence, with the continuous development, the random flow persistently possesses the $-5/3$ slope. Further downstream at x_5 , x_6 and x_7 , both $E(f)$ and f_c continuously decay, but the $-5/3$ slope is kept; however, the bandwidth decreases continuously. In this sense, the flow downstream of x_3 behaves similar to the free decaying turbulence.

The observed PSV here in the Newtonian fluid excludes the possibility of temporally random but spatially smooth chaotic flow (elastic turbulence, normally observed with non-Newtonian fluids in macroscale at very low Re), which requires $E(f)$ decay faster than f^{-3} [21,22]. Compared with previous chaotic flows, the $-5/3$ spectrum in a microchannel with low Re is a novel observation. Therefore, the μEKT is different from the temporal random but spatial smooth chaotic flows.

Normally, $-5/3$ slope is in the inertial subrange that ends at $(f/U) * \eta \approx 0.1$ [24,25], and beyond $-5/3$ spectrum, $E(f)$ decays exponentially. From Fig. 2, η is estimated to be $5 \mu\text{m}$ at x_4 . This scale is at least one order smaller than the channel width. This could support why the span of $E(f)$ with $-5/3$ slope can be one decade wide. In addition, in Fig. 2 beyond $-5/3$ spectrum, $E(f)$ has an averaged slope of -6.3 , which is within the range between -5.2 [25] and -7.2 [26] in high Re turbulence.

D. Scaling exponents of p^{th} order moment of velocity structures

In physical space, velocity structure function $\Delta u(l) = u(x+l) - u(x)$ ($l = U_b \Delta t$, is the spatial length scale and Δt is the time interval) at high Re has the following scaling relation: $\langle |\Delta u(l)|^p \rangle \sim l^{\xi_p}$, where ξ_p is the scaling exponent of p^{th} order moment. According to Kolmogorov's second similarity hypothesis (K41), $\xi_p = p/3$. For low p , ξ_p is close to $p/3$ and the scaling relation of $\Delta u(l)$ matches K41 theory well, but for high

[Title]

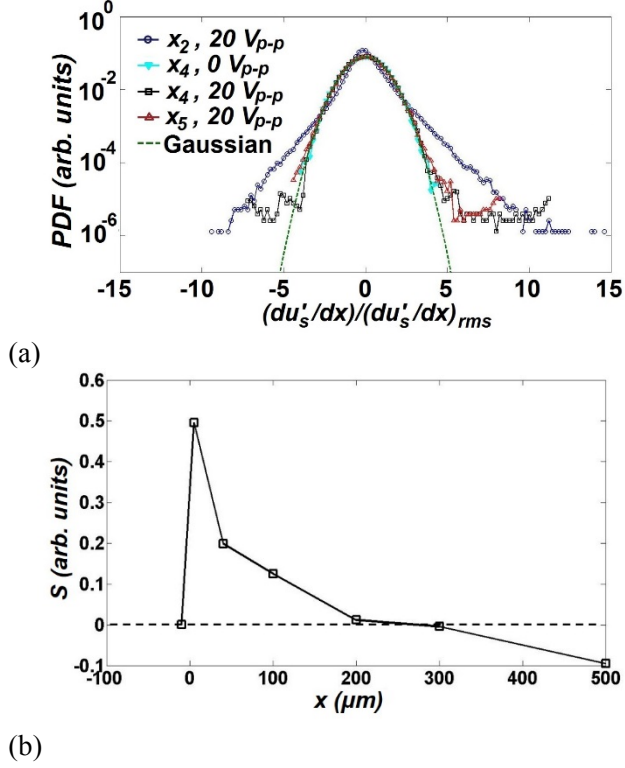


Fig. 4 (Color online) *PDF* and *S* along *x*-direction. (a) *PDF* of $(du'_s/dx)/(du'_s/dx)_{rms}$ at x_3, x_4 and x_5 . (b) *S* of velocity gradients calculated along *x*-direction.

p, ζ_p is lower than $p/3$, i.e. deviates from K41 prediction because of the intermittency of dissipation structure. When u_s is used to represent u , a similar relationship between ζ_p and p is also observed at $20 V_{p-p}$ in the inertial subrange regions at two different x -positions along $y = z = 0$, as shown in Fig. 3a. For $p \leq 4$, the measured ζ_p is very close to K41 prediction. For example, at $p = 3$, the scaling exponent ζ_p is close to 1.01 for all two positions, consistent to the predicted value (1.00) from K41.

However, for $p \geq 4$, the difference between K41 prediction and measured ζ_p increases with increasing p . For instance, at $p = 6$, the measured ζ_p are 1.52 and 1.62 at x_4 and x_5 respectively, which are smaller than both K41 law and the experimental result in high Re

turbulence by Benzi et al [27]. This could indirectly imply F_e has an effect on flow structures, where σ is non-uniform, and thus, causes the intermittency and the departure from known models (such as K41, etc.). The existence of the scaling law region is plotted in Fig. 3b to show the quality of the scaling in real space. Under the three different p , although restricted by the channel

size, the power-law region seems to persist. Therefore, Fig. 3 implies the existence of self-similarity of velocity structures in the μEKT .

E. Probability density function of velocity gradients

Another feature of high Re turbulence is the existence of an exponential tail of probability density function (*PDF*) of the velocity derivative in physical space also due to intermittency at small scales. *PDF* of $(du'_s/dx)/(du'_s/dx)_{rms}$ (equivalent to $(du'_s/dt)/(du'_s/dt)_{rms}$) is investigated at various x -positions, as given in Fig. 4a. Without forcing, the measured *PDF* caused by the noise of the detector is consistent to the Gaussian distribution. With forcing at x_2 , there is a clear exponential tail, corresponding to the small-scale eddies shown in Fig. 2. The tails persist in at x_4 and x_5 , although they are weaker compared with that at x_2 , indicating fast diffusion and dissipation are smearing the smaller structures. This is identical with the PSV shown in Fig. 2.

F. Skewness of velocity gradients

To understand the energy cascade mechanism, we also measured the skewness of velocity gradient, i.e. $S = \langle (du'_s/dx)^3 \rangle / \langle (du'_s/dx)^2 \rangle^{3/2}$, which is closely related to small-scale structures. In Fig. 4b, S is positive upstream of $x = 280 \mu\text{m}$ and then become negative downstream. This is consistent with the exponential tail of *PDF* in Fig. 4a, which is not symmetric, but biased towards the positive side. This behavior is apparently different from the well-known results that in high Re turbulence at small scales, S is mostly negative. In that case, $S < 0$ indicates the energy cascades from large to small scales unidirectionally [28] when an equilibrium state is reached and no external energy is injected. However, in the μEKT where F_e continually contributes to the kinetic energy of flow on a wide range of scales, $S < 0$ is not necessary. The production rate of vorticity is not dominated by the vortex stretching alone [28], but also F_e . Similar results has also been observed in Magnetohydrodynamic turbulence [29].

According to Karman-Howarth (K-H) equation in conventional turbulence, we have $S < 0$, since it is dominated by dissipation term at small scales. However, the conventional K-H equation describes turbulence which is only dominated by inertial term without external force F . To evaluate the influence of F on S , Yakhot [30] suggested a general expression about the

3rd order moment of velocity structure in high-Rayleigh-number Bénard convection as:

$$S_3(l) = -\frac{4}{5}\varepsilon_u l + 6\nu \frac{\partial S_2(l)}{\partial l} + \frac{6}{l^4} \int_0^l l'^4 \langle \Delta u(l') \Delta F(l') \rangle dl' \quad (13)$$

Here we can see if there is no F , the expression turns back to K-H equation. However when F exists, such as \mathbf{F}_e in the present investigation, $S_3(l)$ may not be negative. In EK flows, σ structures, as carriers of \mathbf{F}_e , could be able to cascade to smaller scales and dominate the velocity fluctuations at the small-scale structures as $Sc \gg 1$. Due to \mathbf{F}_e at small scales and incompressibility, a positive correlation between $F_e = |\mathbf{F}_e|$ and u_s is thus possible, i.e. $\langle \Delta u_s(l') \Delta F_e(l') \rangle > 0$. Or in other words, $\langle \Delta u(l') \Delta F_e(l') \rangle \sim l'^{\xi}$, with $\xi < 0$ (where ξ is a scaling exponent). In this case, the 3rd term on the right side of the Eq. (13) can be estimated as:

$$6 \int_0^l l'^4 \langle \Delta u_s(l') \Delta F_e(l') \rangle dl' / l^4 \sim l^{1+\xi} \quad (14)$$

As $\xi < 0$, the sign of $S_3(l)$ is more significantly affected by the external forcing term that can have a positive sign. If $\xi \ll 0$, $S_3(l)$ can become positive even at a larger scale. As du'_s/dx is dominated by small-scale velocity structures, their contribution can cause $S_3(l)$ to become positive. This is another characteristic of the μ EKT that differs from that in the high Re turbulence. Evolution of S along x -direction indicates this μ EKT is not fully developed turbulence.

V. Discussion and Summary

As explained previously[7], the criteria used to determine whether the present highly fluctuated unsteady EK flow is turbulent or not, are based on the common features of turbulence cited in the classical book from Tennekes and Lumley[31]. In addition, one of the major differences between the present μ EKT and the chaotic flows is that, the slope of the power spectrum in the chaotic flows is -3 or steeper, whereas the slope in the μ EKT is -5/3 or less steeper. The newly developed LIFPA provides such a capability to measure the spectrum with ultrahigh spatiotemporal resolution. Because of the nature of microchannels, the observed local μ EKT is already very interesting for fundamental study of fluid dynamics although we only focus on the small range of the first 500 μ m from the entrance,

where the flow exhibits some interesting features. For mixing enhancement, turbulence in such a small range is more than enough to cause mixing of two fluids rapidly to generate chemical reaction for many applications in Lab-on-a-Chip.

Currently, one of our major concerns is whether the energy cascade is direct or inverse. Beyond x_2 , the PSV starts to move to low f region. There can be two reasons: viscous dissipation of the small-scale structures and inverse cascade. If the cascade process is inverse, there could be expected a peak or distinguish signal in $E(f)$ at 100 kHz since f_f is 100 kHz. However, when the sampling rate of 1 MHz (the maximum for the sampling system) is used, an initial peak around f_f and the decay of this peak with its spreading to the low frequency downstream have not been observed, although our LIFPA's temporal resolution should be sufficiently high to measure a 100 kHz signal, if it exists. Also as discussed before [7], a high f_f may not play a key role on the spectra, since high frequency signal in $E(f)$ can also be observed when f_f is only 15 Hz. Thus, the power law should not be caused by the inverse cascade from 100 kHz. From power spectra and visualization within initial 40 μ m downstream of the trailing edge, we can observe both large and small eddies. This may indicate the external energy input is directly accepted by the flow, and converted into both large and small unstable eddies that form at frequencies lower than 100 kHz. The large ones are cascaded into the small ones rapidly, a direct energy cascade process initially. However, inverse cascade is not completely excluded, since $S > 0$ as shown in Fig. 4b. Therefore, both direct and inverse cascade may be involved in the flow. In addition, because the flow is forced throughout the entire sidewalls, it is not clear if the negative viscosity effect [32,33], may also play a role in the cascade process of the μ EKT.

As LIFPA is a 1D single-point measurement method, it cannot distinguish the velocity directions, similar to a single-wire HWA, which is widely used in non-homogeneous and anisotropic flows, such as turbulent boundary layers. For HWA, a single wire probe is more accurate than previously thought and even more precise than a X-wire probe for the 1D spectra measurement when the transverse velocity is considered[25,34]. In addition, when the spectrum of the streamwise velocity component had a power-law region, the slope of the power-law (i.e. scaling law) region of the streamwise spectrum would not be affected by the flow disturbance in transverse directions[34]. This evaluation for HWA can be properly applied to LIFPA. The error caused by

the cross flow for velocity measurement has been investigated recently [8]. It is found that LIFPA introduces even less error since it is noninvasive and the z-direction velocity should have a much less influence on the spectra measurement because of fast photobleaching of the dyes [8]. Therefore, $E(f)$ measurement with LIFPA could be reliable.

If the temporal spectrum is used to explain spatial eddy structures, we need to know whether the Taylor Hypothesis (T-H) can be applied for the present μ EKT. As we know, T-H normally requires the turbulent intensity to be small. We consider position at x_4 as an example to address this issue. At x_4 , the turbulent intensity u_{rms}/U is 37%. Based on Ewing's evaluation of the non-uniform convection error in measurements using T-H [34], if u_{rms}/U is about 31% in atmospheric boundary layers, the estimated relative error in the inertial range of the 1D spectra with a single wire probes of HWA is less than 11%. In the light of Ewing's theory, we estimate that the error of the power-law slope is less than 12%. Therefore, although the velocity in the transverse direction is relatively high, the T-H seems still to be approximately applicable to the present μ EKT.

On one hand, the spectra, structure function and PDF all indicate that the low Re EK flow can exhibit some features of high Re turbulence. However, it is not yet clear if the observed $-5/3$ scaling would be universal in μ EKT flows. On the other hand, since Re_λ under forcing is lower than one, the observed μ EKT seems not to satisfy the conventional scaling relation, i.e. $\eta/\lambda \sim Re_\lambda^{-1/2}$. This should not be a surprise, since Re should not be the only major parameter for the scaling, but also Gr_e (or Ra_e), similar to the role of thermo-Rayleigh number (Ra) in turbulent Rayleigh-Bénard convection [35], where the scaling relies on Ra , which is nonlinearly proportional to Re . Note that while the gravitational force is active on large-scale structures, the electric force in electrokinetic instabilities is mostly active only at interfaces and on small-scale structures. However, the electrokinetic force can still be much larger than the viscous force to generate turbulence when the electric Grashof number is sufficiently high. This is because the total volume of the microchannel is small and the interfacial force can play an important role, although the local interfacial force may be less significant in macroflows, where an interfacial force could be too small to drive a relatively large volume of fluid. In addition, after generation of small structures of conductivity, there will be more interfaces between two

fluids having different conductivity as shown in Fig. 1e. Thus the electric force can be still effective even at small scales as long as there is electric conductivity gradient between the interfaces of small scales.

Compared with turbulent Rayleigh-Bénard convection where Re is also very high for the high Ra , Re in the microfluidic EK flow is very low. Even if $\langle u_s \rangle$ under forcing is larger than that without forcing and may increase with voltage (but decreases downstream) as noticed before [7], Re based on measured $\langle u_s \rangle$, normal and constant value of the water viscosity (note this number could be smaller due to, e.g. Joule heating to increase Reynolds number, but we do not know its real value so far) and inlet width of the microchannel, is estimated not higher than 10 in the entire flow field, which is still very low. Being noted, the Reynolds number used above are all based on conventional definitions and parameters measured. However, if we consider a nominal electric Reynolds number based on U_e and ν , i.e. $Re_e = U_e w / \nu = \sqrt{Gr_e}$, which is the denominator of the last term in Eq. (11), the magnitude of Re_e could be larger than 100. Nevertheless, the experimentally measured u_s is much smaller than U_e used in Eq. (11), and the relevant length scale for the conductivity gradient, what the EK force relies on, is far shorter than d used in the definition of Gr_e . Therefore, although Re_e is not small, its relevance for the μ EKT is yet to be understood. At the present stage, it is not clear which Reynolds number could describe the behaviors of the μ EKT properly. In addition, although the observed μ EKT could be interesting, its mechanism is so far not yet clear and detailed comparison with conventional turbulence is yet to be investigated. For instance, the effect of f_j is not understood yet.

One of the major reasons why the observed μ EKT exhibits some features of high Re flow could be related to the ratio of the forces (and their resultant flows) in the streamwise direction to that in the transverse direction. In moderate Reynolds number flows, the shear force in the streamwise direction is large, and cause the corresponding flows to be more anisotropic. In low Reynolds number flows, normally walls of channels increase viscous shear force, which in turn, also causes flows to be more anisotropic. However, the effects of these shear forces that cause anisotropic flows can be relatively decreased if a force in the transverse direction is exerted and a highly disturbed flow is correspondingly generated in the transverse direction. As discussed in the theory section, compared with the EK force in the transverse direction at the interface between the two streams, the viscous force in

streamwise direction because of the wall should be much smaller in the μ EKT. In the present μ EKT, the flow inertia force and viscous shear force are relatively small because of the low bulk velocity. Therefore, the flow could be less anisotropic when the pressure-driven flow is electrokinetically forced and the generated convection caused by the forcing is in the transverse direction, i.e. orthogonal to the bulk flow. Here we assume the flow becomes less anisotropic, compared with the unforced flow because of the presence of the $-5/3$ spectrum, although the μ EKT may not be homogeneous

In addition, since turbulence is still an unsolved problem, the observed μ EKT may bring some new aspects to turbulence research and could help understand the mechanism of universal behavior of small-scale structures in high Re turbulence. The work provides a new perspective of turbulence, fundamental study of flow in microfluidics, and avenues for control of flow and transport phenomena in Lab-on-a-Chip.

We appreciate discussions with Rui Qiao, Haitao Xu and Laurent Mydlarski. The work was supported by NSF under grant no. CAREER CBET-0954977, MRI CBET-

1040227 and NSF EPSCoR award, EPS-1317771, respectively.

- [1] A. N. Kolmogorov, Dokl. Akad. Nauk SSSR **30** (1941).
- [2] J. P. Brody, P. Yager, R. E. Goldstein, and R. H. Austin, Biophysical Journal **71**, 3430 (1996).
- [3] C.-C. Chang and R.-J. Yang, Microfluid Nanofluid **3**, 501 (2007).
- [4] J. C. Baygents and F. Baldessari, Physics of fluids **10**, 301 (1998).
- [5] C.-H. Chen, H. Lin, S. K. Lele, and J. G. Santiago, Journal of Fluid Mechanics **524**, 261 (2005).
- [6] J. D. Posner and J. G. Santiago, Journal of Fluid Mechanics **555**, 1 (2006).
- [7] G. Wang, F. Yang, and W. Zhao, Lab Chip **14**, 1452 (2014).
- [8] W. Zhao, F. Yang, J. Khan, K. Reifsnider, and G. Wang, Experiments in Fluids **56**, 39 (2015).
- [9] H. Hu and M. M. Koochesfahani, Measurement Science and Technology **17**, 1269 (2006).
- [10] M. M. Koochesfahani and D. G. Nocera, *Molecular Tagging Velocimetry. Handbook of Experimental Fluid Dynamics. Chapter 5.4* (Springer-Verlag, 2007), Chapter 5.4.
- [11] N. T. Nguyen, Flow Meas. Instrum. **8**, 7 (1997).
- [12] A. M. C. Van Dinter, C. G. P. H. Schroën, F. J. Vergeldt, R. G. M. Van der Sman, and R. M. Boom, Advances in Colloid and Interface Science **173**, 23 (2012).
- [13] A. Voigt, C. Bayer, K. Shirai, L. Büttner, and J. Czarske, Applied Optics **47**, 5028 (2008).
- [14] C. Kuang, W. Zhao, F. Yang, and G. Wang, Microfluidics and Nanofluidics **7**, 509 (2009).
- [15] A. Ramos, H. Morgan, N. G. Green, and A. Castellanos, Journal of Physics D: Applied Physics **31**, 2338 (1998).
- [16] G. Xie, J. Luo, S. Liu, C. Zhang, and X. Lu, Tribology Letters **29**, 169 (2008).
- [17] See Supplemental Material at [URL will be inserted by publisher] for visualization videos of unforced flow, forced flows at $V_f = 8 V_{p-p}$ and $V_f = 20 V_{p-p}$ respectively.
- [18] C. Kuang, R. Qiao, and G. Wang, Microfluid Nanofluid **11**, 353 (2011).
- [19] C. Kuang and G. Wang, Lab-on-a-Chip **10**, 240 (2010).
- [20] A. A. Joneidi, G. Domairry, and M. Babaelahi, Commun Nonlinear Sci Numer Simulat **15**, 3423 (2010).
- [21] T. Burghlea, E. Segre, and V. Steinberg, Phys Rev Lett **92**, 164501 (2004).
- [22] A. Groisman and V. Steinberg, Nature **405**, 53 (2000).
- [23] K. R. Sreenivasan, Physics of Fluids **8**, 189 (1996).
- [24] S. Chen, G. Doolen, J. R. Herring, R. H. Kraichnan, S. A. Orszag, and Z. S. She, Physical Review Letters **70**, 3051 (1993).
- [25] S. G. Saddoughi and S. V. Veeravalli, Journal of Fluid Mechanics **268**, 333 (1994).
- [26] G. Comte-Bellot and S. Corrsin, Journal of Fluid Mechanics **48**, 273 (1971).
- [27] R. Benzi, L. Biferale, S. Ciliberto, M. V. Struglia, and R. Tripiccion, Physica D **96**, 162 (1996).
- [28] A. S. Monin and A. M. Yaglom, *Statistical fluid mechanics* (MIT Press, Cambridge, Massachusetts, 1975), Vol. II.
- [29] O. Zikanov and A. Thess, Journal of Fluid Mechanics **358**, 299 (1998).
- [30] V. Yakhot, Physical Review Letters **69**, 769 (1992).
- [31] H. Tennekes and J. L. Lumley, *A First Course in Turbulence* (The MIT press, 1972).
- [32] G. Sivashinsky and V. Yakhot, Physics of Fluids **28**, 1040 (1985).
- [33] L. Shtilman and G. Sivashinsky, Journal de Physique **47**, 1137 (1986).
- [34] D. Ewing, Experiments in Fluids **36**, 675 (2004).
- [35] D. Lohse and K.-Q. Xia, Annual Review of Fluid Mechanics **42**, 335 (2010).